bioRxiv preprint doi: https://doi.org/10.1101/2020.12.09.418632; this version posted December 11, 2020. The copyright holder for this preprint (which was not certified by peer review) is the author/funder, who has granted bioRxiv a license to display the preprint in perpetuity. It is made available under aCC-BY-NC-ND 4.0 International license.

Title: Dual color mesoscopic imaging reveals spatiotemporally heterogeneous coordination of cholinergic and neocortical activity.

Authors: Sweyta Lohani[1,*], Andrew H. Moberly[1,*], Hadas Benisty[1], Boris Landa[2], Miao Jing[3], Yulong Li[4], Michael J. Higley[1,#], and Jessica A. Cardin[1,#]

Affiliations:
[1] Department of Neuroscience, Kavli Institute for Neuroscience, Yale University School of Medicine, New Haven, CT 06510 USA
[2] Program in Applied Mathematics, Yale University, New Haven, CT 06510 USA
[3] Chinese Institute for Brain Research, Beijing, 102206, China
[4] State Key Laboratory of Membrane Biology, Peking University School of Life Sciences; PKU-IDG/McGovern Institute for Brain Research; Peking-Tsinghua Center for Life Sciences, Beijing 100871, China

[*] These authors contributed equally to this work.
[#] These authors share primary correspondence for this work.

Lead Contacts: jess.cardin@yale.edu, m.higley@yale.edu

Abstract

Acetylcholine (ACh) is associated with the modulation of brain activity linked to arousal, attention, and emotional valence. We performed dual-color mesoscopic imaging of ACh and calcium across the neocortex of awake mice to investigate the spatiotemporal dynamics of cholinergic signaling and their relationship to cortical output. We find distinct movement-defined behavioral states are represented in spatially heterogeneous cholinergic networks that are differentially coupled to fluctuations in local circuit activity.

bioRxiv preprint doi: https://doi.org/10.1101/2020.12.09.418632; this version posted December 11, 2020. The copyright holder for this preprint (which was not certified by peer review) is the author/funder, who has granted bioRxiv a license to display the preprint in perpetuity. It is made available under aCC-BY-NC-ND 4.0 International license.

Animals cycle through multiple waking brain states that profoundly influence patterns of neuronal activity, perception, and behavior[1-3]. Classical views suggest these states reflect brain-wide, homogeneous influence of ascending neuromodulatory systems[4]. For example, cholinergic neurons in the basal forebrain send widespread projections throughout the neocortex that are thought to contribute to the effects of arousal, attention, and emotional valence on cortical dynamics[5-8]. However, recent electrophysiological and anatomical studies indicate substantial diversity in the firing patterns and axonal arborizations of cholinergic neurons, suggesting their output may be spatially and temporally heterogeneous in different cortical areas[9-12]. Currently, the spatiotemporal dynamics of cholinergic signaling across the cortex and their relationship to specific behavioral states are unknown. Motor activity (e.g., running, whisking) provides a robust metric for categorizing behavioral states and is richly represented in the neocortex, shaping both spontaneous and sensory-evoked firing[13, 14]. Here, we used two-color, wide-field "mesoscopic" imaging[15] of genetically-encoded reporters for calcium and ACh in the awake mouse to quantify the relationship between behavioral state, cortical activity, and cholinergic signaling. Our results provide strong evidence that ACh dynamics are highly variable across cortical areas and are differentially coupled to local circuit activity across distinct categories of motor behavior.

To simultaneously monitor neuronal activity and cholinergic signaling in the neocortex of awake mice, we expressed the red fluorescent calcium indicator jRCaMP1b[16] and the green fluorescent ACh sensor ACh3.0[17] throughout the brain via neonatal injection of AAV vectors into the transverse sinus[18, 19]. This approach resulted in cortex-wide, uniform expression of both reporters, and we confirmed both *ex vivo* and *in vivo* that ACh3.0 specifically reported cholinergic signaling (Figure S1). We then performed mesoscopic imaging of both reporters through the intact skull of mice that were head-fixed and freely running on a wheel (Figure 1a, see Methods). Imaging was performed by strobing 570nm (jRCaMP1b), 470nm (ACh3.0), and 395nm (control) excitation light with an overall frame rate of 10 Hz per channel. ACh3.0 and jRCaMP1b images were co-registered, aligned to the Allen Common Coordinate Framework (CCFv3)[20], and normalized ($\Delta F/F$). We removed hemodynamic and motion-related artifacts using a novel regression approach that leverages spatial correlations in signal and noise and takes advantage of reduced ACh-sensitive fluorescence of ACh3.0 when excited at 395nm[17] (Figure S1, see Methods). This method outperformed conventional pixel-wise regression in its ability to remove stimulus-induced negative transients in green fluorescence corresponding to hemodynamic absorption[21, 22] for both ACh3.0 and GFP (Figure S2).

Both ACh and calcium signals exhibited spatially heterogeneous, spontaneous fluctuations across the cortex (Figure 1b,c). To investigate the relationship of this activity to behavior, we tracked the animal's state using a combination of facial movements, pupil area, wheel running speed, and electrocorticogram (ECoG). Sustained periods of elevated arousal (locomotion, facial movement) were associated with modest changes in the average cholinergic and calcium signals (Figure S3). However, state transition points were associated with transients in both signals (Figure S4). To illustrate the continuous temporal relationship between behavioral state and neural dynamics, we highlighted data from two spatially distant cortical areas, primary visual cortex (V1) and the supplemental motor area (M2). Overall, large fluctuations in activity occurred simultaneously across cortical regions for both cholinergic and calcium signals and co-varied with changes in pupil dilation, locomotion,

bioRxiv preprint doi: https://doi.org/10.1101/2020.12.09.418632; this version posted December 11, 2020. The copyright holder for this preprint (which was not certified by peer review) is the author/funder, who has granted bioRxiv a license to display the preprint in perpetuity. It is made available under aCC-BY-NC-ND 4.0 International license.

facial movement, and high-frequency ECoG activity (Figure 1c). However, spatially varied patterns in both channels were evident during specific periods of arousal and quiescence (highlighted time frames), supporting a model in which ACh release is both dynamic and heterogeneous across cortical regions.

We quantified the relationships between behavioral variables and fluorescence activity using a cross-validated linear regression model that included facial movements (FaceMap principal components 1-25), locomotion speed, pupil diameter, or ECoG as predictors of ACh or calcium fluctuations for each CCFv3-defined parcel. For both signals, facial movements provided the best overall prediction accuracy (R^2), with other variables contributing markedly less predictive power (Figure 1d-e, Figure S5). These results are consistent with variable coupling of ACh to subsets of waking behavioral states, rather than simply signaling non-specific arousal levels. We also observed a striking spatial difference in the coupling between behavior and fluctuations in ACh and cortical activity. Facial movement was most strongly predictive of cholinergic activity in frontal regions, but most predictive of calcium activity in posterior regions (Figure 1d), and similar results were found for other state variables (Figure 1e, Figure S5). Moreover, a similar anterior-posterior gradient was observed for signals evoked by behavioral state transitions (Figure S4).

We next examined the spatial coordination of ACh and calcium signals by measuring pairwise correlations between cortical regions, focusing on sustained (>5 seconds) periods of either locomotion versus quiescence or high versus low facial movement activity in the absence of locomotion (see Figure S3). We found that locomotion was associated with a marked reduction in the between-area correlations of cholinergic activity that was broadly significant across the cortex (Figure 2a, left). In contrast, calcium signals exhibited a significant locomotion-associated increase in correlation for somatosensory areas, with minimal change for frontal or visual regions (Figure 2a, right). Distinct from locomotion, increased facial movement was associated with a spatially heterogeneous increase in correlations for cholinergic activity and a broad increase in correlations for calcium signals (Figure 2b, left and right).

Finally, we quantified the relationship between cholinergic and calcium signals across the cortex as a function of behavioral state. Locomotion was associated with a significant reduction in correlation between the two channels that was restricted to the frontal cortex (Figure 3a-b). In striking contrast, facial movement in the absence of locomotion was associated with a significant increase in correlation between the two signals broadly across the cortex (Figure 3c-d). Overall, our data demonstrate a spatially compartmentalized relationship between cholinergic modulation and cortical activity that is diversely dependent on spontaneous fluctuations in movement-defined behavioral states.

Prior to our study, experimental examination of competing hypotheses about cholinergic dynamics was limited by experimental challenges to monitoring ACh release and neural activity *in vivo* across multiple cortical regions simultaneously with high spatial and temporal resolution. We solved this problem using mesoscopic imaging of calcium (via jRCaMP1b) and ACh (via ACh3.0) across the dorsal cortex in behaving mice. Our results clearly demonstrate that cholinergic signaling exhibits substantial spatiotemporal variation that is differentially coupled to distinct behavioral states, defined by patterns of motor activity. Indeed, behavioral variables are more strongly predictive of cholinergic signaling in the anterior cortex, in contrast to calcium signals that are more

bioRxiv preprint doi: https://doi.org/10.1101/2020.12.09.418632; this version posted December 11, 2020. The copyright holder for this preprint (which was not certified by peer review) is the author/funder, who has granted bioRxiv a license to display the preprint in perpetuity. It is made available under aCC-BY-NC-ND 4.0 International license.

strongly linked to state in posterior regions. We also find that locomotion drives significant cortex-wide decorrelation of ACh activity and decouples it from calcium activity selectively in the frontal cortex, emphasizing the independence of cholinergic signals across the cortex. In contrast, increased facial movements occur with enhanced spatial correlations of calcium signals and a strengthening of their relationship to cholinergic activity. Our results are consistent with earlier work showing that firing of cholinergic axons in V1 tracks fluctuations in motor activity, though we find only a weak relationship with pupil dilation[23]. Overall, our findings underscore the view that waking comprises diverse behavioral states characterized by specific patterns of neural and neuromodulatory dynamics[3, 4].

We emphasize that ACh3.0 fluorescence serves as a proxy for cholinergic modulation, reporting the spatiotemporal patterns of ACh release[17]. However, as the reporter is expressed non-selectively in neurons, it does not provide information regarding the physiological extent of ACh reception or cell type-specific downstream signaling. In this way, our approach is similar to imaging of cholinergic axons[23] or electrochemical measurement of cholinergic release[24] but capable of stable, longitudinal monitoring across the entire dorsal cortex in the absence of invasive probes.

In conclusion, we provide novel evidence for the idea that movement is broadly represented in the cortex, not only in local circuit activity[13, 14] but also in the dynamics of cholinergic modulation. Additional studies are required to determine whether these common patterns reflect movement-related ascending regulation of cortical networks or top-down, state-dependent control of basal forebrain output[4]. In either case, we propose the broad hypothesis that the fine-tuned orchestration of behavioral and cortical state dynamics requires coordinated coupling of neuronal activity and cholinergic modulation within distinct, spatially heterogeneous networks of the neocortex.

bioRxiv preprint doi: https://doi.org/10.1101/2020.12.09.418632; this version posted December 11, 2020. The copyright holder for this preprint (which was not certified by peer review) is the author/funder, who has granted bioRxiv a license to display the preprint in perpetuity. It is made available under aCC-BY-NC-ND 4.0 International license.

Author Contributions

SL, AHM, MJ, YL, MJH, and JAC designed the experiments. SL and AHM collected the data. SL, AHM, HB, and BL analyzed the data. SL, AHM, MJH, and JAC wrote the manuscript.

Acknowledgements

The authors thank all members of the Higley and Cardin laboratories for helpful input throughout all stages of this study. We thank Rima Pant for generation of AAV vectors. We thank Daniel Barson, Gal Mishne, and Ronald Coifman for helpful discussions regarding the analysis of the data. We thank Quentin Perrenoud for providing the locomotion changepoint analysis code. We thank the GENIE Project for jRCaMP1b plasmids. This work was supported by funding from the NIH (MH099045 and MH121841 to MJH, EY022951 to JAC, MH113852 to MJH and JAC, EY031133 to AHM, EY026878 to the Yale Vision Core), an award from the Kavli Institute of Neuroscience (to MJH and JAC), a Simons Foundation SFARI Research Grant (to MJH and JAC), support from the Ludwig Foundation (to JAC), and an award from the Swartz Foundation (to HB).

Conflicts of Interest

The authors declare no conflicts of interest exist.

bioRxiv preprint doi: https://doi.org/10.1101/2020.12.09.418632; this version posted December 11, 2020. The copyright holder for this preprint (which was not certified by peer review) is the author/funder, who has granted bioRxiv a license to display the preprint in perpetuity. It is made available under aCC-BY-NC-ND 4.0 International license.

Figure Legends

Figure 1. Spatiotemporal dynamics of cholinergic and neural activity in the neocortex. **a**, Schematic of the dual wavelength, widefield imaging setup. **b**, Example representative image frames showing fluctuations in cholinergic (ACh3.0, top row) and neural (jRCaMP1b, bottom row) activity across the dorsal cortical surface. Overlaid lines indicate Allen Brain CCFv3-derived parcellation of V1 and M2. **c**, Time series for ACh3.0 and jRCaMP1b signals in V1 (red) and M2 (purple) parcels. Instantaneous (3 s window) Pearson's correlation (R) between V1 and M2 is shown in gray. Simultaneous pupil area, running speed, facial motion (FaceMap PC1), and ECoG power spectrogram are shown below. Dashed lines indicate time of frames in (a). **d**, Average spatial map (n=6 mice) showing ten-fold cross-validated explained variance (R^2) of ACh3.0 (left) and jRCaMP1b (right) signals based on facial movement (FaceMap PC1-25). Individual animal values and population medians are shown for V1 and M2. * indicates $p<0.05$, paired t-test, n=6 mice. **e**, Same as in (d) for explained variance of ACh3.0 (left) and jRCaMP1b (right) signals based on locomotion.

Figure 2. State-dependent variation in spatial correlations of cholinergic and neural activity. a, Average peak cross-correlation matrices (n=6 mice) for cholinergic (ACh3.0, left) and calcium (jRCaMP1b, right) activity during locomotion (top) and quiescence (center), measured pairwise for CCFv3-defined cortical parcels in the left hemisphere. Average difference in correlation between locomotion and quiescence is shown for significant pairs (bottom, adjusted $p<0.01$, Benjamini-Yekutieli FDR corrected permutation test). Non-significant pairs are shown in gray. **b**, As in (a) for high (top) and low (center) periods of facial movement (FaceMap PC1) in the absence of locomotion. Differences for significant pairs are shown (bottom).

Figure 3. State-dependent spatial variation in correlations between cholinergic and calcium signals. a, Average maps (n=6 mice) showing peak cross-correlation coefficients between ACh3.0 and jRCaMP1b activity for each cortical parcel during quiescence (left) and locomotion (center). **b**. Difference in correlations for significant parcels are shown (right, adjusted $p<0.01$, Benjamini-Yekutieli FDR corrected permutation test). Non-significant parcels are shown in gray. **(c, d)** Same as (a) and (b) for high and low periods of facial movement (FaceMap PC1) in the absence of locomotion.

bioRxiv preprint doi: https://doi.org/10.1101/2020.12.09.418632; this version posted December 11, 2020. The copyright holder for this preprint (which was not certified by peer review) is the author/funder, who has granted bioRxiv a license to display the preprint in perpetuity. It is made available under aCC-BY-NC-ND 4.0 International license.

References

1. McGinley, M.J., *et al.* Waking State: Rapid Variations Modulate Neural and Behavioral Responses. *Neuron* **87**, 1143-1161 (2015).
2. Niell, C.M. & Stryker, M.P. Modulation of visual responses by behavioral state in mouse visual cortex. *Neuron* **65**, 472-479 (2010).
3. Vinck, M., Batista-Brito, R., Knoblich, U. & Cardin, J.A. Arousal and locomotion make distinct contributions to cortical activity patterns and visual encoding. *Neuron* **86**, 740-754 (2015).
4. Lee, S.H. & Dan, Y. Neuromodulation of brain states. *Neuron* **76**, 209-222 (2012).
5. Chubykin, A.A., Roach, E.B., Bear, M.F. & Shuler, M.G. A cholinergic mechanism for reward timing within primary visual cortex. *Neuron* **77**, 723-735 (2013).
6. Picciotto, M.R., Higley, M.J. & Mineur, Y.S. Acetylcholine as a Neuromodulator: Cholinergic Signaling Shapes Nervous System Function and Behavior. *Neuron* **76**, 116-129 (2012).
7. Poulet, J.F.A. & Crochet, S. The Cortical States of Wakefulness. *Front Syst Neurosci* **12**, 64 (2018).
8. Sarter, M. & Lustig, C. Cholinergic double duty: cue detection and attentional control. *Curr Opin Psychol* **29**, 102-107 (2019).
9. Laszlovszky, T., *et al.* Distinct synchronization, cortical coupling and behavioral function of two basal forebrain cholinergic neuron types. *Nat Neurosci* **23**, 992-1003 (2020).
10. Li, X., *et al.* Generation of a whole-brain atlas for the cholinergic system and mesoscopic projectome analysis of basal forebrain cholinergic neurons. *Proc Natl Acad Sci U S A* **115**, 415-420 (2018).
11. Munoz, W. & Rudy, B. Spatiotemporal specificity in cholinergic control of neocortical function. *Curr Opin Neurobiol* **26**, 149-160 (2014).
12. Zaborszky, L., *et al.* Neurons in the basal forebrain project to the cortex in a complex topographic organization that reflects corticocortical connectivity patterns: an experimental study based on retrograde tracing and 3D reconstruction. *Cereb Cortex* **25**, 118-137 (2015).
13. Musall, S., Kaufman, M.T., Juavinett, A.L., Gluf, S. & Churchland, A.K. Single-trial neural dynamics are dominated by richly varied movements. *Nat Neurosci* **22**, 1677-1686 (2019).
14. Stringer, C., *et al.* Spontaneous behaviors drive multidimensional, brainwide activity. *Science* **364**, 255-+ (2019).
15. Cardin, J.A., Crair, M.C. & Higley, M.J. Mesoscopic Imaging: Shining a Wide Light on Large-Scale Neural Dynamics. *Neuron* **108**, 33-43 (2020).
16. Dana, H., *et al.* Sensitive red protein calcium indicators for imaging neural activity. *Elife* **5** (2016).
17. Jing, M., *et al.* An optimized acetylcholine sensor for monitoring in vivo cholinergic activity. *Nat Methods* (2020).
18. Barson, D., *et al.* Simultaneous mesoscopic and two-photon imaging of neuronal activity in cortical circuits. *Nat Methods* **17**, 107-113 (2020).
19. Hamodi, A.S., Martinez Sabino, A., Fitzgerald, N.D., Moschou, D. & Crair, M.C. Transverse sinus injections drive robust whole-brain expression of transgenes. *Elife* **9** (2020).
20. Wang, Q., *et al.* The Allen Mouse Brain Common Coordinate Framework: A 3D Reference Atlas. *Cell* **181**, 936-953 e920 (2020).
21. Ma, Y., *et al.* Wide-field optical mapping of neural activity and brain haemodynamics: considerations and novel approaches. *Philos Trans R Soc Lond B Biol Sci* **371** (2016).
22. Valley, M.T., *et al.* Separation of hemodynamic signals from GCaMP fluorescence measured with wide-field imaging. *J Neurophysiol* **123**, 356-366 (2020).
23. Reimer, J., *et al.* Pupil fluctuations track rapid changes in adrenergic and cholinergic activity in cortex. *Nat Commun* **7**, 13289 (2016).
24. Sarter, M. & Kim, Y. Interpreting chemical neurotransmission in vivo: techniques, time scales, and theories. *ACS Chem Neurosci* **6**, 8-10 (2015).

bioRxiv preprint doi: https://doi.org/10.1101/2020.12.09.418632; this version posted December 11, 2020. The copyright holder for this preprint (which was not certified by peer review) is the author/funder, who has granted bioRxiv a license to display the preprint in perpetuity. It is made available under aCC-BY-NC-ND 4.0 International license.

Materials and Methods:

Animals

Male and female C57BL/6J mice were kept on a 12h light/dark cycle, provided with food and water ad libitum, and housed individually following headpost implants. Imaging experiments were performed during the light phase of the cycle. All animal handling and experiments were performed according to the ethical guidelines of the Institutional Animal Care and Use Committee of the Yale University School of Medicine.

Neonatal sinus injections

Brain-wide expression of ACh3.0 and jRCaMP1b was achieved via postnatal sinus injection[18, 19]. Specifically, P0-P1 litters were removed from their home cage and placed on a heating pad. Pups were kept on ice for 5 min to induce anesthesia via hypothermia and then maintained on a metal plate surrounded by ice for the duration of the injection. Under a dissecting microscope, two small incisions were made in the skin over the transverse sinuses. Viral injections were made with a NanoFil (WPI) attached to a 36 gauge needle and an UltraMicroPump (WPI) mounted to a stereotaxic arm. The needle was slowly lowered through the skull into the underlying transverse sinus. Pups were injected bilaterally with 2 ul of AAV9-hsyn-ACh3.0 (1-8x10^13 gc/ml) and 2 ul of AAV9-hsyn-jRCaMP1b (2.5x10^13 gc/ml, Addgene). A subset of pups were bilaterally injected with 4 ul AAV9-hsyn-EGFP (3.4x10^13 gc/ml, Addgene). Viruses were injected at 10 nl/s, and the needle was left in the sinus for 30 s following the injection. Incision sites were sealed with Vetbond glue, and pups were moved to a heating pad. Once the entire litter was injected, pups were gently rubbed with home cage bedding and nesting material and returned to their home cage.

Surgical procedures

All surgical implant procedures were performed on adult mice (>P50). Mice were anesthetized using 1-2% isoflurane and maintained at 37ºC for the duration of the surgery. The skin and fascia above the skull were removed from the nasal bone to the posterior of the intraparietal bone and laterally between the temporal muscles. The surface of the skull was thoroughly cleaned with saline and the edges of the incision secured to the skull with Vetbond. A custom titanium headpost was secured to the posterior of the nasal bone with transparent dental cement (Metabond, Parkell), and a thin layer of dental cement was applied to the entire dorsal surface of the skull. Next, a layer of cyanoacrylate (Maxi-Cure, Bob Smith Industries) was used to cover the skull and left to cure ~30 min at room temperature to provide a smooth surface for transcranial imaging.

For simultaneous ECoG implants, a dental drill was used to make a small craniotomy (~1mm) lateral to V1 in the right hemisphere. A silver ball electrode was placed in the craniotomy and a teflon coated silver reference wire implanted in the contralateral cerebellar hemisphere. A ground wire was wrapped around a skull screw placed in the ipsilateral intraparietal bone. For simultaneous basal forebrain stimulation in a subset of animals, stainless steel bipolar stimulating electrodes (125 um diameter, Invivo1) were implanted at the following coordinates (AP = -0.5 mm, ML = 1.6 mm, DV = 4 mm, angle = 0 degrees or AP = -0.5 mm, ML = 3.3 mm, DV =

bioRxiv preprint doi: https://doi.org/10.1101/2020.12.09.418632; this version posted December 11, 2020. The copyright holder for this preprint (which was not certified by peer review) is the author/funder, who has granted bioRxiv a license to display the preprint in perpetuity. It is made available under aCC-BY-NC-ND 4.0 International license.

3.7 mm, angle = 20 degrees) to target the nucleus basalis in the right hemisphere. Stimulation comprised a brief burst at 100 Hz (1 ms pulse width, 20 pulses, 60-100 uA). Desynchronization in cortical ECOG was used to verify correct electrode placement and to titrate the stimulation intensity.

Widefield imaging

Widefield calcium and cholinergic imaging was performed using a Zeiss Axiozoom with a PlanNeoFluar Z 1x, 0.25 numerical aperture objective with a 56 mm working distance. Epifluorescent excitation was provided by an LED bank (Spectra X Light Engine, Lumencor) using three output wavelengths: 395/25, 470/24, and 575/25 nm. Emitted light passed through a dual camera image splitter (TwinCam, Cairn Research) then through either a 525/50 or 630/75 emission filter (Chroma) before it reached two sCMOS cameras (Orca-Flash V3, Hamamatsu). Images were acquired at 512x512 resolution after 4x pixel binning, and each channel was acquired at 10 Hz with 20 ms exposure. Images were saved to a solid state drive using HCImage software (Hamamatsu).

Backscatter illumination was provided by LEDs (Thorlabs M530L4, M625L4) centered and narrowly filtered at 530 nm and 625 nm coupled to a 1000 um diameter bifurcated fiber (BFY1000LS02) that terminated 45 degrees incident to the brain surface. Image frames capturing backscatter at 530 and 625 nm were acquired at 10 Hz and interleaved with the usual fluorescence emission acquisition.

All imaging was performed in awake, behaving mice that were head-fixed so that they could freely run on a cylindrical wheel. A magnetic angle sensor (Digikey) attached to the wheel continuously monitored wheel motion. Mice received at least three wheel-training habituation sessions before imaging to ensure consistent running bouts. During widefield imaging sessions, the face (including the pupil and whiskers) was illuminated with an IR LED bank and imaged with a miniature CMOS camera (Blackfly s-USB3, Flir) with a frame rate of 10 Hz. To monitor the ECoG, we used a DP-311A differential amplifier with active headstage (Warner Instruments). Signals were amplified 1000x, filtered between 0.1Hz and 1000 Hz, and digitized at 5000 Hz using a Power 1401 acquisition board (CED).

Visual stimulation and air-puffs

During backscatter imaging sessions, small (40 degree diameter) sinusoidal drifting gratings (2 Hz, 0.04 cycles/degree, 100% contrast) were generated using Psychtoolbox in Matlab and presented on an LCD monitor at a distance of 20 cm from the right eye. Stimuli were presented for 2 seconds with a 5 second inter-stimulus interval. Air-puff stimuli were delivered using a thin metal tube aimed at the fur along the back and coupled to a solenoid valve (Clark Solutions) that delivered brief (200 ms) puffs of compressed air.

Histology

Histological validation was performed on a subset of animals at the conclusion of imaging experiments. Mice were deeply anesthetized with isoflurane and perfused transcardially with phosphate buffered saline (PBS) followed by 4 percent paraformaldehyde in PBS. Brains were postfixed overnight at 4 degrees and embedded

bioRxiv preprint doi: https://doi.org/10.1101/2020.12.09.418632; this version posted December 11, 2020. The copyright holder for this preprint (which was not certified by peer review) is the author/funder, who has granted bioRxiv a license to display the preprint in perpetuity. It is made available under aCC-BY-NC-ND 4.0 International license.

in 1% agarose, and 50 um sagittal sections were cut on a vibratome (VT1000, Leica). Slices were pretreated in blocking solution (2 percent normal goat serum, 0.1 percent Triton X-100 in PBS) for four hours then incubated with primary antibodies at 1:1000 (rabbit anti-GFP and guinea pig anti-NeuN, Invitrogen) at 4 degrees for 24 hours. The following day, slices were washed with PBS and incubated in secondary antibodies (anti-rabbit-Alexa Fluor 488 and anti-guinea pig-Alexa Fluor 647, Invitrogen) at 1:1000 for two hours at room temperature. Slices were washed 3 times in PBS then mounted on glass slides in Vectashield antifade mounting medium (Vector Laboratories). Epifluorescent images were acquired on an Olympus BX53 fluorescence microscope. Confocal images were taken with a Zeiss LSM 710.

ACh3.0 imaging *ex vivo*

Under isoflurane anesthesia, mice were decapitated and coronal slices (~300 um thick) were cut in ice-cold external solution containing (in mM): 100 choline chloride, 25 NaHCO3, 1.25 NaH2PO4, 2.5 KCl, 7 MgCl2, 0.5 CaCl2, 15 glucose, 11.6 sodium ascorbate and 3.1 sodium pyruvate, bubbled with 95% O2 and 5% CO2. Slices were transferred to artificial cerebrospinal fluid (ACSF) containing (in mM): 127 NaCl, 25 NaHCO3, 1.25 NaH2PO4, 2.5 KCl, 1 MgCl2, 2 CaCl2 and 15 glucose, bubbled with 95% O2 and 5% CO2. After an incubation period, slices were moved to a modified recording chamber under the objective of the widefield microscope and constantly perfused with oxygenated ACSF. Slices were imaged using the same protocol as during *in vivo* imaging sessions (10 Hz, 20 ms exposure). A glass pipette filled with 20 millimolar carbachol was mounted in a micromanipulator and lowered to just above the slice. A Picospritzer (Parker Hannifin Corp) was used to deliver 200 ms puffs of carbachol. During some trials, scopolamine (20 uM) was added to the ACSF before carbachol puffs were applied.

Data analysis

All analyses were conducted using custom-written scripts in MATLAB (Mathworks).

Preprocessing of imaging data

512x512 images were down-sampled to 256x256, and frames were grouped by excitation wavelength (395 nm, 470 nm, 575 nm). For dual color imaging, green and red images were acquired using different cameras and registered via automatic ‘rigid’ transformation using imregtform in MATLAB. In some cases, registration points were manually selected and a ‘similarity’ geometric transformation was applied. Images were then detrended and baseline corrected to calculate $\Delta F/F$ images. Specifically, for each pixel, a 100th order fir1 filter with 0.001 Hz frequency cutoff was applied to extract the low pass filtered signal. This low pass signal was used as baseline (F0), and $\Delta F/F$ for each pixel was calculated as (F- F0)/F0, where F is the raw unfiltered signal. $\Delta F/F$ values were used for all subsequent analyses. Images were registered to the Allen Common Coordinate framework (CCFv3) using manually selected control points and ‘similarity’ based geometric transformation. Time series for individual brain parcels were then extracted by averaging $\Delta F/F$ values across all pixels within a parcel.

bioRxiv preprint doi: https://doi.org/10.1101/2020.12.09.418632; this version posted December 11, 2020. The copyright holder for this preprint (which was not certified by peer review) is the author/funder, who has granted bioRxiv a license to display the preprint in perpetuity. It is made available under aCC-BY-NC-ND 4.0 International license.

Hemodynamics correction

Common methods for correction of hemodynamic artifacts are typically based on linear regression of a neural activity-dependent signal against an activity-independent signal and performed on a pixel-by-pixel basis, ignoring the spatial correlations among neighboring pixels that exist within and between the two signals. However, accounting for such correlations can be advantageous for mitigating the effects of noise. We experimentally confirmed that excitation of ACh3.0 with 395 nm light results in fluorescence with substantially reduced dependence on ACh (Figure S1), enabling us to use this approach to correct the signal collected with 470 nm excitation. We now present our mathematical formulation for hemodynamic artifact removal as the optimal linear predictor for the neuronal time series, given the 470 nm- and 395 nm- excitation signals.

Let y_1 and y_2 be $p \times 1$ random signals corresponding to p pixels of the 470 nm and 395 nm signals, respectively. Let x and z be mutually uncorrelated $p \times 1$ random signals corresponding to p pixels of the ACh-dependent and -independent (hemodynamic) signals, respectively. We consider the following linear model:

$$y_1 = x + z + \eta,$$
$$y_2 = Az + \xi,$$

where η and ξ are white Gaussian $p \times 1$ noise signals and A is an unknown $p \times p$ real invertible matrix. Given the above-mentioned model, our goal is to estimate the signal x.

It can be verified that the optimal linear estimator of x in the sense of Minimum Mean Squared Error (MMSE) is given by:

$$\hat{x} = H\begin{pmatrix} y_1 \\ y_2 \end{pmatrix}, \quad H = \Sigma_{xy}\Sigma_y^{-1},$$

Where $y = \begin{pmatrix} y_1 \\ y_2 \end{pmatrix}$ is given by stacking y_1 on top of y_2, $\Sigma_y = \mathbb{E}[yy^T]$ is the autocorrelation matrix of y, and $\Sigma_{xy} = \mathbb{E}[xy^T]$ is the cross-correlation matrix between x and y. While Σ_y can be estimated directly from the observations, this is not trivially the case for Σ_{xy} since it depends on the unknown signal x. Nevertheless, we show below that Σ_{xy} can be expressed as:

$$\Sigma_{xy} = \left(\Sigma_{y_1} - \sigma_\eta^2 I - \left(\Sigma_{y_1y_2}\left(\Sigma_{y_2} - \sigma_\xi^2 I\right)^{-1}\Sigma_{y_2}^{-1}\Sigma_{y_1y_2}^T\right)^T \quad 0\right),$$

Where σ_η^2 and σ_ξ^2 are the noise variances of η and ξ, respectively, and I is the $p \times p$ identity matrix. Importantly, all quantities in the formula for Σ_{xy} can be estimated directly from the observations of y_1 and y_2. The noise variances σ_η^2 and σ_ξ^2 were evaluated according to the median of the singular values of the corresponding correlation matrices Σ_{y_1} and Σ_{y_2}.

Proof for the formula for Σ_{xy}:

$$\Sigma_{xy} = (\Sigma_{xy_1} \quad \Sigma_{xy_2})$$
$$\Sigma_{xy_1} = \Sigma_x$$
$$\Sigma_{xy_2} = 0$$

bioRxiv preprint doi: https://doi.org/10.1101/2020.12.09.418632; this version posted December 11, 2020. The copyright holder for this preprint (which was not certified by peer review) is the author/funder, who has granted bioRxiv a license to display the preprint in perpetuity. It is made available under aCC-BY-NC-ND 4.0 International license.

$$\Sigma_{y_1} = \Sigma_x + \Sigma_z + \Sigma_\eta$$

$$\Sigma_{y_2} = A\Sigma_z A^T + \Sigma_\xi$$

$$\Sigma_{y_1 y_2} = \Sigma_z A^T$$

Using these equations, we can extract $\Sigma_z = \left(\Sigma_{y_1 y_2}\left(\Sigma_{y_2} - \Sigma_\xi\right)^{-1}\Sigma_{y_2}^{-1}\Sigma_{y_1 y_2}^T\right)^T$ which leads to:

$$\Sigma_{xy_1} = \Sigma_{y_1} - \Sigma_\eta - \left(\Sigma_{y_1 y_2}\left(\Sigma_{y_2} - \Sigma_\xi\right)^{-1}\Sigma_{y_2}^{-1}\Sigma_{y_1 y_2}^T\right)^T$$

Note that in the case of a single pixel, i.e. $p = 1$, our estimator reduces to a simple regression based on pixelwise correlations. However, taking p to be all pixels at once is both computationally expensive and unnecessary. Therefore, we performed these evaluations locally, where the time trace of each pixel was computed based on a patch of its nearest spatial neighbors. The size of the patch was determined according to the amount of time samples available. Using a bigger patch would lead to bigger covariance matrices to be estimated and therefor requires longer time traces. For our sessions a patch size of 9×9 was empirically selected as most adequate.

Validation of hemodynamics correction

The novel spatial regression approach used here was validated by comparing results with other known hemodynamics correction strategies. Several benchmarks were used to determine the effectiveness of our method. First, we and others have observed that strong stimuli, such as a high-contrast visual stimulus, evoke negative dips in fluorescence signals that are driven by hemodynamic photon absorption [21, 22]. Here, we compared this visual stimulus-evoked negativity for uncorrected ΔF/F signals (measured for 470 nm excitation) and ΔF/F signals corrected by either spatial or pixel-wise regression of signals collected at 395 nm excitation. Visual trials were Z-score normalized to the -2 to 0 s pre-stimulus period, and the minimum Z-scored values at 0 to 5 s after stimulus onset were calculated for each trial. These values were then averaged across all trials in an animal, and statistical comparisons were made within mice between the three methods using protected paired t-tests following repeated measures ANOVA. A complementary approach involves the measurement of hemodynamic absorption from changes in the reflectance ("backscatter") of green photons while simultaneously performing fluorescence imaging [21, 22]. Here, we carried out pixel-wise and spatial regression of Ach 3.0 signals using 530 nm backscatter data and compared results with 395 nm-based correction. Finally, we also assessed the efficiency of the different correction approaches to reduce the variance in ΔF/F signals collected from GFP-expressing control mice, where all fluctuations are assumed to result primarily from hemodynamic variation. Statistical comparisons on Z-score maximum negativity values post-air-puff were performed in a similar manner as descried above for visual stimuli.

Preprocessing of behavior data

Facial movements were extracted from face videography using FaceMap[14]. The toolbox applies singular value decomposition (SVD) to the face movie to extract the 1000 dimensions or principal components (PCs) that

bioRxiv preprint doi: https://doi.org/10.1101/2020.12.09.418632; this version posted December 11, 2020. The copyright holder for this preprint (which was not certified by peer review) is the author/funder, who has granted bioRxiv a license to display the preprint in perpetuity. It is made available under aCC-BY-NC-ND 4.0 International license.

explain the distinct movements apparent on the mouse's face. Here, we included the top 25 PCs for regression analyses and the first PC for other analyses. To extract face movement change points, we focused on quiescence periods only, because locomotion is consistently associated with increased facial motion. First, PC1 data were Z-score normalized within a session, and the high/low thresholds corresponding to 60% and 40% quantiles in the data distribution during quiescence only were extracted for that session. Data were then smoothed using a 1s-window moving average filter, and epochs during which smoothed data continuously exceeded the high/low Z-threshold for at least 0.5 s were considered high/low face state, respectively.

Wheel position was determined from the output of the linear angle detector. The circular wheel position variable was first transformed to the [-π,π] interval. The phases were then circularly unwrapped to get running distance as a linear variable, and locomotion speed was computed as a differential of distance (cm/s). A change-point detection algorithm detected locomotion onset/offset times based on changes in standard deviation of speed. First, moving standard deviations of speed were computed in 2 s windows, which was the temporal resolution of the changepoint analysis. Initial locomotion onset/offset times were then estimated from periods when the moving standard deviations exceeded/ fell below an empirical threshold of 0.005. These estimates were refined by computing the time points corresponding to the maximum of the moving forward/backward Z-score in 2 s windows around each onset/offset time. Locomotion epochs that were too short (<1s) or where average speed was too low (<2 cm/s) were removed.

ECoG processing

From the raw ECOG signal, the power spectral density (PSD) was computed in 1 s windows using MATLAB's *periodogram* function. For each window, the bandpower was calculated by integrating the PSD over a frequency range of 30 to 100 Hz. For display purposes, the multitaper spectrogram was estimated from the raw ECOG signal using the Chronux toolbox (using sliding windows of 3 s with 0.5 s overlap).

Post-processing analysis

Imaging data from individual parcels were used for subsequent analyses. While computations were performed for all Allen CCFv3 parcels, the primary visual cortex (V1) and the secondary motor area in the frontal cortex (M2) were selected as representative areas for some population summaries and statistical comparisons.

Regression with behavioral variables

Linear regression was used to predict ACh3.0 and jRCaMP1b activity in each parcel using behavioral variables as predictors. MATLAB's *cvpartition* function was used for 10 fold cross-validation. The prediction accuracy was calculated on testing data in each of the 10 folds and averaged to get a final cross-validated R^2. Individual regression models were built using 25 FaceMap PCs, pupil area, wheel speed, or ECoG. Statistical comparisons were performed between cross-validated R^2 values for V1 and M2 within mice using paired t-tests.

Trial averaged activity

bioRxiv preprint doi: https://doi.org/10.1101/2020.12.09.418632; this version posted December 11, 2020. The copyright holder for this preprint (which was not certified by peer review) is the author/funder, who has granted bioRxiv a license to display the preprint in perpetuity. It is made available under aCC-BY-NC-ND 4.0 International license.

Basal forebrain stimulation: Trials where basal forebrain stimulation caused locomotion were automatically excluded. Data were Z-score normalized to the pre-stimulus period -2 to 0 s. Z-scored data were averaged across all trials across all animals and presented as mean +/- standard error of mean across trials. Locomotion onset: Only locomotion trials that contained at least 5 s of running and were preceded by a minimum 10 s of quiescence were included for trial averages. Data were Z-score normalized to the pre-locomotion period of -5 to -3 s, and Z-scored data were averaged across all trials for each animal. High face state onset: If a high face state (see behavioral data preprocessing) was preceded by at least 4 s of a low face state, the transition between the two states was used as the high state onset time point. To get trial averages around face state transitions, trials were Z-score normalized to the -4 to -2 s baseline period and averaged across all trials for each animal. Statistical comparisons were performed on peak Z-score evoked activity at 0 to 1 s after locomotion/high face onset between V1 and M2 within mice using paired t-tests.

State-dependent correlations

Time-lagged correlations between every pair of Allen CCF parcels in Ach 3.0 or jRCaMP1b signals were computed by performing cross-correlations with 500 ms time lag and extracting the maximum correlation coefficient. The resulting parcel-wise correlation matrices were calculated during sustained behavioral states with a minimum duration of 5 s to allow enough time frames for lagged correlations. In addition, it was required that for sustained locomotion states, locomotion started at least 3 s before or ended at least 3 s after the state boundaries. Similarly, for sustained quiescence states, it was required that any locomotion did not occur at least 10 s before and 10 s after a given period. To characterize these states, the mean and coefficient of variation of imaging data in V1 were computed and compared between locomotion and quiescence or high and low face/pupil states using paired t-tests.

To ensure accurate comparison in correlations between states, the number of state epochs and total duration within each epoch were matched for locomotion versus quiescence and high versus low facial movement periods within each session. Then, correlation matrices were calculated for each state epoch and averaged all epochs and sessions for each animal to get one correlation matrix per animal per state. Cross-correlations between Ach 3.0 and jRCaMP1b activity for distinct behavioral states were calculated in a similar manner except the correlations were performed between the two signals within areas. To assess the significance of differences in pairwise correlations between states, a stratified permutation test was used. In each permutation, state labels were shuffled across epochs within each animal, and the corresponding correlation matrices were averaged across all epochs of a particular state to get one permuted correlation matrix per state per animal. These values were then averaged across animals to get a mean difference between states. This was repeated 10,000 times to build a null distribution of mean differences which was compared against the observed mean difference to determine p-values. Multiple comparisons correction was performed by setting the false discovery rate (FDR) to $q < 0.01$ and using Benjamini-Yekutieli method in fdr_bh.m toolbox in MATLAB.

bioRxiv preprint doi: https://doi.org/10.1101/2020.12.09.418632; this version posted December 11, 2020. The copyright holder for this preprint (which was not certified by peer review) is the author/funder, who has granted bioRxiv a license to display the preprint in perpetuity. It is made available under aCC-BY-NC-ND 4.0 International license.

Supplemental Figure Legends

Figure S1. Viral expression of the cholinergic reporter ACh3.0. a, Example widefield (top) and confocal (bottom) fluorescent images from an adult mouse expressing RCaMP1b and ACh3.0 following neonatal virus injection. Scale bars; 1mm top, 25 μm, bottom. **b**, Example brain slice from a ACh3.0-expressing mouse imaged with 470nm (blue) and 395 (violet) excitation light on interleaved frames. Images show fluorescence at baseline (left) and 20 second after (right) carbachol (20 μM) was puffed onto the slice. Scale bar; 1mm. **c**, Peak carbachol-evoked ΔF/F responses for 395nm versus 470nm excitation, in control saline or in the presence of scopolamine (10 μM). **d**, Schematic showing bipolar stimulation electrodes implanted in the basal forebrain (left) and corresponding mesoscopic image (right). Scale bar; 1mm. **e,** Average spatial maps of Z-scored ACh3.0 signal before (left) and after (right) electrical stimulation of the basal forebrain. **f,** Mean +/- SEM (n=8 sessions, 3 mice) Z-scored ACh3.0 signals activity evoked by electrical stimulation for V1 (red) and M2 (purple) parcels indicated in (e). Corresponding changes in locomotion, pupil, facial movement (FM PC1), and ECoG are illustrated below.

Figure S2. Spatial regression for correction of hemodynamic artifacts in mesoscopic data. a, ACh3.0 signals measured in V1, illustrating different hemodynamic correction methods. **b,** Z-scored average ACh3.0 activity evoked by visual stimulation at times indicated in (a). Traces are for uncorrected fluorescence (blue) and images corrected using pixel-wise regression of 395nm fluorescence data (purple) or 530nm back-scatter data (green), or spatial regression of 395nm (red) or 530 (orange) data. **c,** Individual animal and population median (n=6 mice) values for Z-scored, visually-evoked negativity (hemodynamic artifact) for the different regression methods. * indicates $p<0.05$, protected paired t-tests following repeated measures ANOVA. **d-f**, as in (a-c) for jRCaMP1b data (n=6 mice) in V1. **g,** Pixel-wise variance remaining from imaging of a GFP-expressing mouse following hemodynamic correction with pixel-wise (left) or spatial (right) regression of 395nm fluorescence data. **h**, Z-scored average GFP fluorescence in V1 evoked by air-puff stimulus to the animal's flank. Traces are for uncorrected fluorescence (blue) and images corrected using pixelwise (purple) or spatial (red) regression of 395nm data. **i**, Individual animal and population median (n=3 mice) values for Z-scored, air-puff-evoked negativity for the different regression methods. * indicated $p<0.05$, protected paired t-tests.

Figure S3. Characterization of sustained movement-defined behavioral states. a, Example traces indicating locomotion and facial movement (FaceMap PC1). Sustained periods of low (red) or high (blue) motor activity are indicated by shaded regions. **b**, Histograms (left) illustrate distribution of fluorescence values for ACh3.0 (top) and jRCaMP1b (bottom) activity in V1 during locomotion in one example mouse. Plots (center and right) indicate population data (n=6 mice) for average and coefficient of variation ΔF/F values for high versus low states. * indicates $p<0.05$ for paired t-tests. **c**. Same as **b**, for facial movement.

Figure S4. State transition-evoked cholinergic and neural activity. a, Spatial maps show example ACh3.0 and jRCaMP1b activity evoked after locomotion onset. Traces show average activity for V1 (red) and M2 (purple)

bioRxiv preprint doi: https://doi.org/10.1101/2020.12.09.418632; this version posted December 11, 2020. The copyright holder for this preprint (which was not certified by peer review) is the author/funder, who has granted bioRxiv a license to display the preprint in perpetuity. It is made available under aCC-BY-NC-ND 4.0 International license.

for one session, with simultaneous locomotion, pupil area, and facial movement (FaceMap PC1) data shown below. Insets indicate population data for evoked signals in V1 and M2. * indicates $p<0.05$, paired t-test. **b**, as in (a) for onset of facial movement.

Figure S5. Differential coupling of behavioral variables to cholinergic and neural activity. **a**, Average spatial map (left, n=6 mice) showing cross-validated explained variance (R^2) of ACh3.0 (left) and jRCaMP1b (right) signals based on pupil area. Individual animal values and population medians are shown for V1 and M2. * indicates $p<0.05$, paired t-test, n=6 mice. **b**, Same as in (a) for explained variance of ACh3.0 (left) and jRCaMP1b (right) based on high frequency ECoG power.

bioRxiv preprint doi: https://doi.org/10.1101/2020.12.09.418632; this version posted December 11, 2020. The copyright holder for this preprint (which was not certified by peer review) is the author/funder, who has granted bioRxiv a license to display the preprint in perpetuity. It is made available under aCC-BY-NC-ND 4.0 International license.

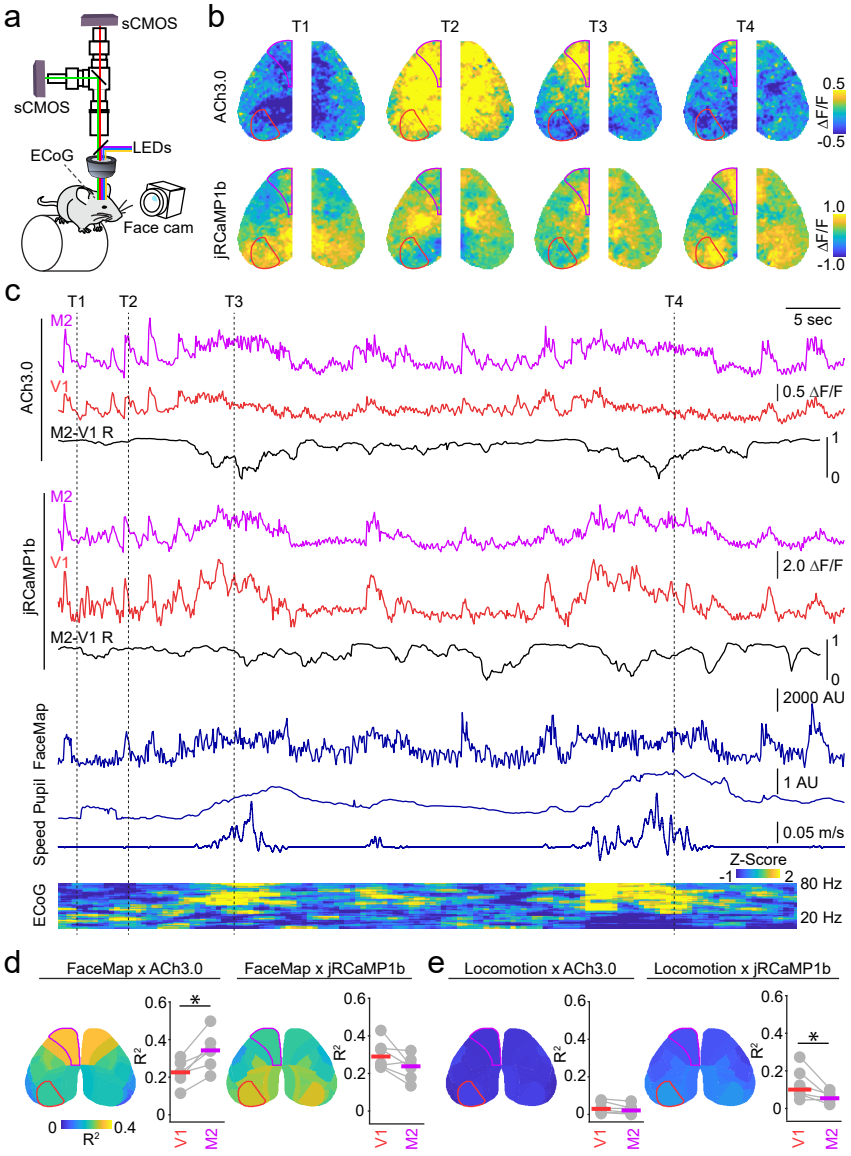

Figure 1

bioRxiv preprint doi: https://doi.org/10.1101/2020.12.09.418632; this version posted December 11, 2020. The copyright holder for this preprint (which was not certified by peer review) is the author/funder, who has granted bioRxiv a license to display the preprint in perpetuity. It is made available under aCC-BY-NC-ND 4.0 International license.

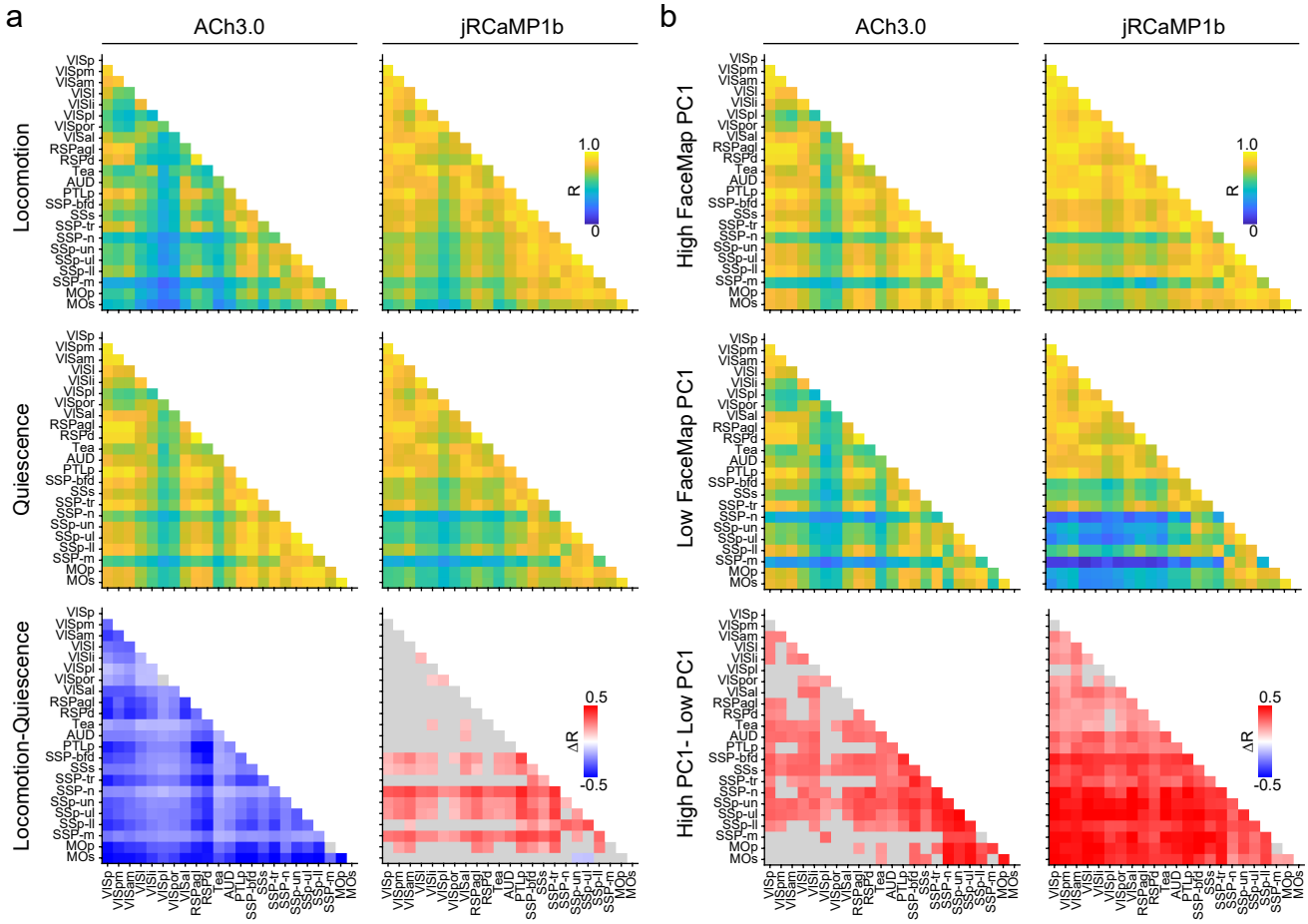

Figure 2

bioRxiv preprint doi: https://doi.org/10.1101/2020.12.09.418632; this version posted December 11, 2020. The copyright holder for this preprint (which was not certified by peer review) is the author/funder, who has granted bioRxiv a license to display the preprint in perpetuity. It is made available under aCC-BY-NC-ND 4.0 International license.

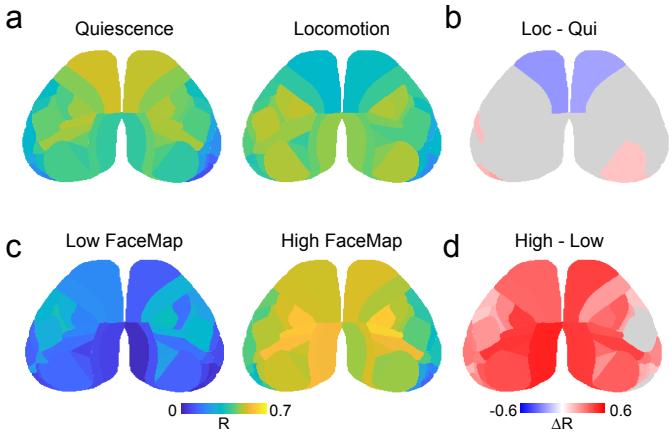

Figure 3

bioRxiv preprint doi: https://doi.org/10.1101/2020.12.09.418632; this version posted December 11, 2020. The copyright holder for this preprint (which was not certified by peer review) is the author/funder, who has granted bioRxiv a license to display the preprint in perpetuity. It is made available under aCC-BY-NC-ND 4.0 International license.

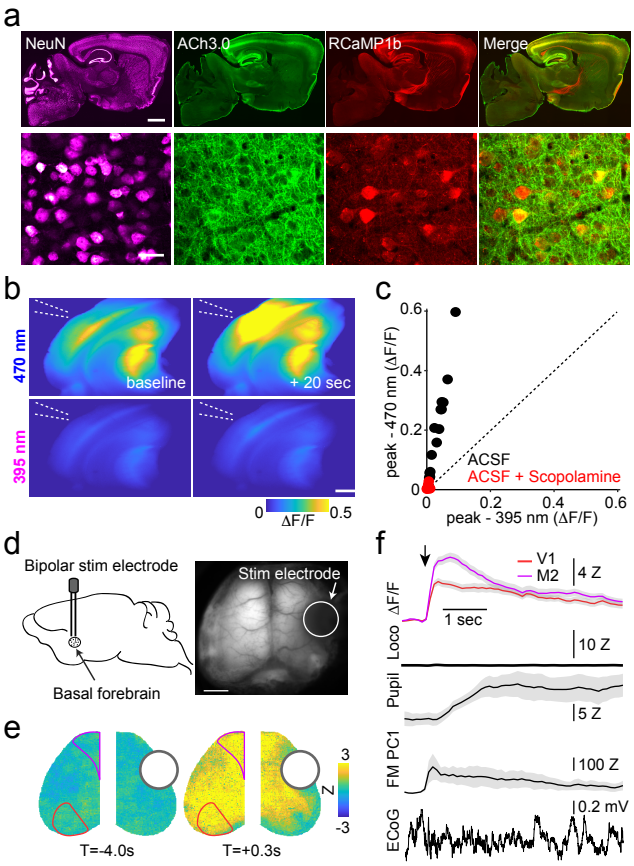

Figure S1

bioRxiv preprint doi: https://doi.org/10.1101/2020.12.09.418632; this version posted December 11, 2020. The copyright holder for this preprint (which was not certified by peer review) is the author/funder, who has granted bioRxiv a license to display the preprint in perpetuity. It is made available under aCC-BY-NC-ND 4.0 International license.

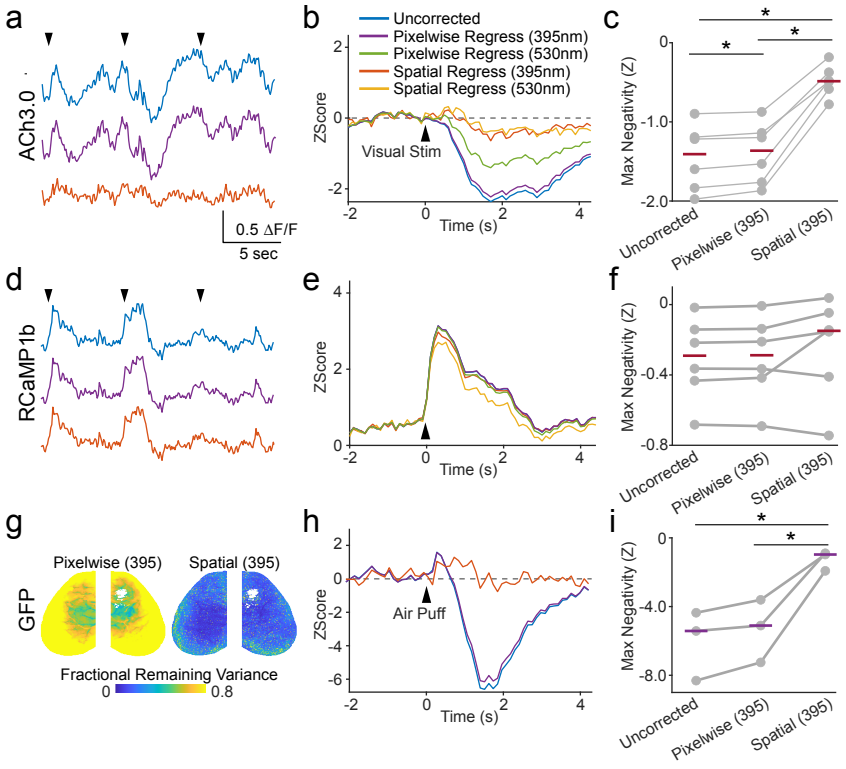

Figure S2

bioRxiv preprint doi: https://doi.org/10.1101/2020.12.09.418632; this version posted December 11, 2020. The copyright holder for this preprint (which was not certified by peer review) is the author/funder, who has granted bioRxiv a license to display the preprint in perpetuity. It is made available under aCC-BY-NC-ND 4.0 International license.

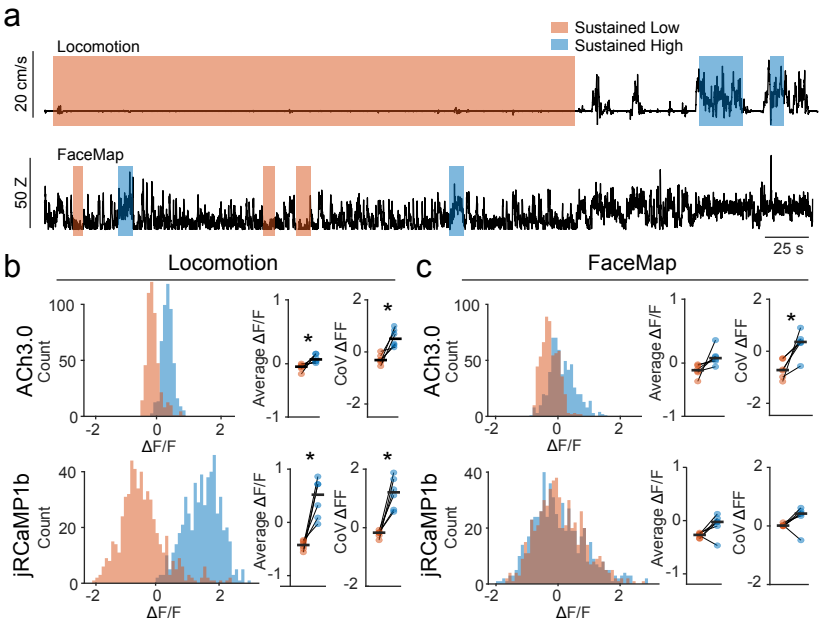

Figure S3

bioRxiv preprint doi: https://doi.org/10.1101/2020.12.09.418632; this version posted December 11, 2020. The copyright holder for this preprint (which was not certified by peer review) is the author/funder, who has granted bioRxiv a license to display the preprint in perpetuity. It is made available under aCC-BY-NC-ND 4.0 International license.

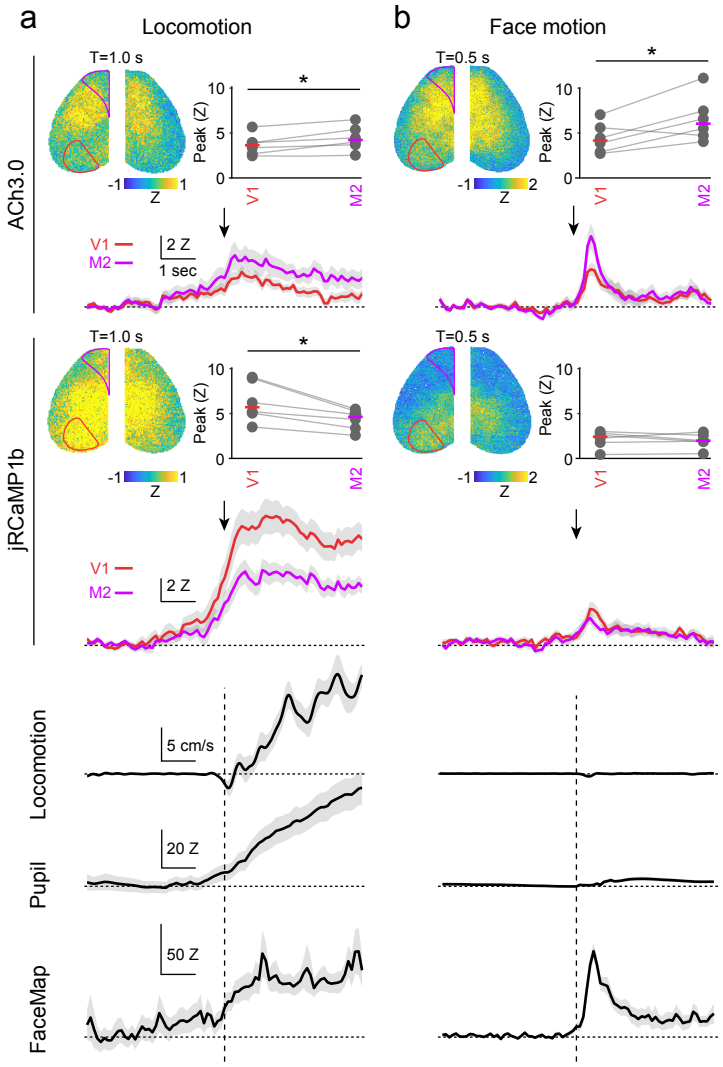

Figure S4

bioRxiv preprint doi: https://doi.org/10.1101/2020.12.09.418632; this version posted December 11, 2020. The copyright holder for this preprint (which was not certified by peer review) is the author/funder, who has granted bioRxiv a license to display the preprint in perpetuity. It is made available under aCC-BY-NC-ND 4.0 International license.

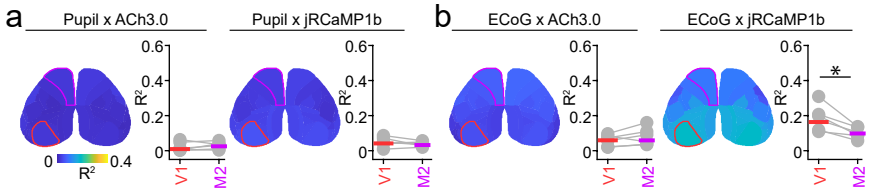

Figure S5